LAWRENCE
LIVERMORE
NATIONAL
LABORATORY

LLNL-JRNL-686300

Electron-Ion Temperature Equilibration in Warm Dense Tantalum

T. Doeppner, S. LePape, T. Ma, A. Pak, N. J. Hartley, L. Peters, G. Gregori, P. Belancourt, R. P. Drake, D. A. Chapman, S. Richardson, D. O. Gericke, S. H. Glenzer, D. Khaghani, P. Neumayer, J. Vorberger, T. G. White

March 18, 2016

High Energy Desnsity Physics

Disclaimer

Electron-Ion Temperature Equilibration in Warm Dense Tantalum

N. J. Hartley[a], P. Belancourt[b], D. A. Chapman[c,d], T. Döppner[e], R. P. Drake[b], D. O. Gericke[d], S. H. Glenzer[f], D. Khaghani[g], S. LePape[e], T. Ma[e], P. Neumayer[g], A. Pak[e], L. Peters[a], S. Richardson[c], J. Vorberger[h], T. G. White[i], G. Gregori[a]

[a]*Department of Physics, University of Oxford, Parks Road, Oxford OX1 3PU, UK*
[b]*Atmospheric, Oceanic, Space Science, University of Michigan, 2455 Hayward St, Ann Arbor, MI 48103, USA*
[c]*Plasma Physics Department, AWE plc., Aldermaston, Reading RG7 4PR, UK*
[d]*Centre for Fusion, Space and Astrophysics, Department of Physics, University of Warwick, Coventry CV4 7AL, UK*
[e]*Lawrence Livermore National Laboratory, 7000 East Avenue, Livermore, California 94550, USA*
[f]*SLAC National Accelerator Laboratory, 2575 Sand Hill Road, Menlo Park, California 94025, USA*
[g]*ExtreMe Matter Institute, GSI Helmholtzzentrum für Schwerionenforschung GmbH, Planckstr. 1, 64291 Darmstadt, Germany*
[h]*Max-Planck-Institut für Physik Komplexer Systeme, 01187 Dresden, Germany*
[i]*Department of Physics, Imperial College London, SW7 2AZ, UK*

Abstract

We present measurements of electron-ion temperature equilibration in proton-heated tantalum, under warm dense matter conditions. Our results agree with theoretical predictions for metals calculated using input data from *ab initio* molecular dynamics simulations. However, the fast relaxation observed in the experiment contrasts with much longer equilibration times found in proton heated carbon, indicating that the energy flow pathways in warm dense matter are far from being fully understood.

1. Introduction

Warm Dense Matter (WDM) is an area of research attracting increasing interest, both in terms of theoretical descriptions [1, 2, 3, 4] and experimental studies [5, 6, 7, 8, 9] . Falling between the better-understood states of condensed matter and plasma, it is characterised by temperatures of ∼1-10 eV and densities near to that of solids. This gives a coupling parameter (*i.e.*, the ratio of the potential to the thermal energy of the ions) of order unity, such that neither the thermal nor potential energy terms can be treated as perturbations to a known solution, as is the case in other regimes. Despite the difficulties, knowledge of WDM is crucial to inertial confinement fusion (ICF) research [10, 11], as well as in the study of exoplanets and other astrophysical objects [12, 13].

In general, experimental studies of WDM use a rapid heating mechanism, with properties of the material probed at timescales comparable to, or even shorter than the timescale of the ionic motion, such that the density is that of the original (pre-heated) solid, while the temperature has risen quickly enough to push the matter into the WDM regime. These mechanisms tend to preferentially heat either the ion subsystem, in the case of shock driven samples [14, 15], or the electron subsystem for illumination by lasers or charged particles. In both of these instances, there is a finite, but poorly known, amount of time needed for the temperatures of the respective subsystems to equilibrate and the material to reach local thermodynamic equilibrium. Only after this time, but before significant expansion and cooling has occurred, can results obtained from the material be meaningfully related to steady-state WDM conditions as those found in planetary cores.

Previous work [16, 17, 18, 19] on charged particle heated electrons in graphite suggests the existence of an energy transfer "bottleneck", although results from volumetric x-ray heating using a free electron laser imply a very rapid equilibration time [20] . This points to an energy exchange process that can depend on the details of the energy distribution of the electrons, or at the very least on the heating mechanism used [21]. Theoretical work based on *ab initio* simulations for the density of states (DOS) [22, 2] indicates that rates in elemental metals are expected to be high, but this remains untested for many materials.

Email address: nicholas.hartley@physics.ox.ac.uk (N. J. Hartley)

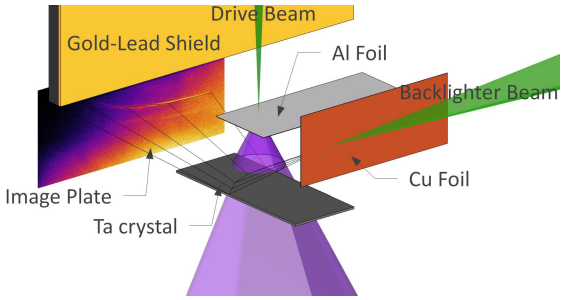

Figure 1: Schematic of setup: the laser beam coming from above drives the proton beam (in purple) from the Al foil which heats the Ta crystal. Meanwhile, the backlighter beam strikes a Cu foil, producing x-rays which diffract from the sample and are detected on the image plate. The gold-lead layered shield prevents direct illumination of the IP by the x-ray source.

Here, we present measurements of the electron-ion coupling strength in tantalum under proton-heated WDM conditions. We find that the rate is much higher than in graphite, as expected, and indeed higher than that measured in other metals. This finding does, however, agree with theoretical predictions and suggests that the model used is applicable in metals under these and similar conditions.

2. Experimental Method

The results presented are from an experiment carried out on the Titan laser at the Jupiter Laser Facility, Larence Livermore National Laboratory (USA). A 10 ps short pulse laser beam, operating at the fundamental wavelength (λ_0=1054 nm), was split in two arms using a pump-probe configuration (see Figure 1). The protons were created by focusing ~40% of the energy (a ~40 J laser beam, which we refer to as the drive beam) onto a thin Al foil in a 50 μm focal spot. This accelerates electrons out of the target, creating a sheath field and driving an intense proton beam out of the rear surface of the aluminium, through the Target Normal Sheath Accleration (TNSA) mechanism [23]. An image of the proton beam as recorded on different layers of a radiochromic film (RCF) detector (Gafchromic EBT2 was used in this experiment) is given in Figure 2.

Half of this proton beam is incident onto a 5 μm thick single-crystal Ta sample, placed between a 30 μm plastic tamper and a silicate substrate. The tamper prevented expansion as well as absorbed the low energy protons ($E \lesssim 1.5$ MeV), giving a spectrum that heats the sample crystal more evenly, and isochorically. The other

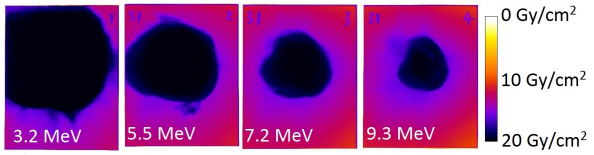

Figure 2: Radiochromic film images of proton areal dose at each layer, and the relevant energy.
This data was taken without sample in place in order to fully characterize the proton beam.

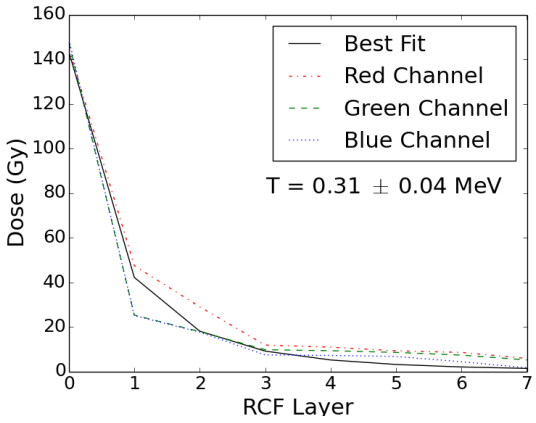

Figure 3: Fitted proton spectrum, shown with spectra derived from the three colour channels of the radiochromic film.

half of the beam was recorded on the RCF pack, which darkens in response to incoming radiation, allowing for an on-shot measurement of the proton fluence [24]. The RCF film is read out by scanning it through visible light with separate color filters. These respond differently to the same dose, as seen in Figure 3. The RCF data is then fitted to a spectrum of the form described by Fuchs *et. al.* [25], and in our case it corresponds to protons with a characteristic temperature of 0.31 ± 0.04 MeV, with the error taken fitting to different colour channels.

The spectrum was used in conjunction with stopping power values taken from the SRIM database to allow calculation of the temporally- and spatially-resolved energy deposition in the sample. Using heat capacities derived from the electron density of states, to be taken from a density functional theory calculation, described below, we find that this corresponded to an average heating rate of ~2 $\times 10^9$ W m^{-3}, and gave a maximum electron temperature of $T_{max} \sim 4$ eV.

While this proton generation and heating was occurring, the remaining laser energy (delivering a ~60 J

probe beam) was focused, with a 30 μm spot diameter, on a thin Cu foil to produce K-α x-rays ($E = 8,047$ keV). These x-rays probed the (200) Bragg peak of the tantalum crystal 70 ps after the heating beam incidence, at an angle of 27.8°. The image plate detector was placed 200 mm away from the sample to achieve a magnification of 93.

3. Data Analysis and Modelling

The intensity of the diffracted x-ray signal changes due to two different effects. As the random motion of the ions increases with temperature, the intensity of the well defined Bragg peaks drops, known as the Debye-Waller effect. Meanwhile, as more bound electrons are progressively ionized, the atomic form factor, F, is reduced, thus decreasing the diffraction strength even further [26]. The change in diffracted intensity can be written as:

$$\frac{I}{I_0} \propto \left|\frac{F}{F_0}\right|^2 e^{-Ck^2\langle u^2\rangle}, \tag{1a}$$

$$\langle u^2\rangle = \frac{3\hbar^2}{Mk_B\Theta_D}\left[\frac{1}{4} + \left(\frac{T_i}{\Theta_D}\right)^2 \int_0^{\Theta_D/T_i} \frac{x dx}{e^x - 1}\right], \tag{1b}$$

where I is the diffracted intensity in the driven sample at an ion temperature T_i, and I_0 is the diffracted intensity in cold (undriven) tantalum. Similarly, F and F_0 are the atomic form factor for the driven and undriven cases, respectively. The Thomas-Fermi equation of state model predicts that in the proton heated tantalum the average ionization is less than 6 [27]. Since the outer electrons contribute little to the total form factor, changes in F are negligible and we can assume $F \sim F_0$. In Eqs. (1a) and (1b), $\langle u^2\rangle$ is the root-mean-square value of the ion position and $k = \frac{2\pi}{\lambda}\sin\left(\frac{\theta_B}{2}\right)$, with λ being the probe x-ray wavelength, θ_B the Bragg angle, M the ion mass, k_B the Boltzmann constant, and θ_D the Debye temperature. The constant C depends on whether the observed diffraction is dynamic, $C = 1$, or kinematic, $C = 2$ [28]. In the situation considered here, of a thick (i.e., multiples larger than the extinction length) perfect crystal, we are well into the dynamic diffraction regime, giving a smaller intensity reduction for the same temperature change.

The relationship described in Eq. (1) then allows the reduction in diffraction signal to be converted into an ion temperature, but relies on knowledge of the Debye temperature, which characterises the potential well around the ions. As we are working with short timescales and a tamper layer to prevent expansion, nearby ions do not have sufficient time to move and change the potential landscape, allowing us to neglect change in Θ_D due to a rise in ion temperature.

To see the effect of T_e, we used the density functional theory (DFT) code Abinit [29, 30, 31]. We apply it for a unit cell, with metallic band occupation and a Fermi-Dirac smearing due to finite-temperature effects. We can then calculate the ion motion as a function of time, with no interspecies energy exchange, and extract the effective potential, and therefore the Debye temperature, that the ions experience. This gives $\Theta_D = 225$ K, with a change in the Debye temperature of around 5% over the range of T_e probed. These changes are well within the other errors, and the value is consequently assumed to be constant.

$$C_e\frac{\partial T_e}{\partial t} = \nabla\cdot\mathbf{K}_e - G(T_e)\cdot(T_e - T_i) + S_R(t) \tag{2a}$$

$$C_i\frac{\partial T_i}{\partial t} = \nabla\cdot\mathbf{K}_i + G(T_e)\cdot(T_e - T_i) \tag{2b}$$

The inferred ion temperature from the decrease in Bragg diffraction intensity can also be compared to the results predicted by a two-temperature model [32], which is frequently used in calculating the temperature evolution in WDM [33]. With the energy deposited into the electrons, $S_R(t)$, given by the proton beam stopping power as discussed in the previous section, the subsequent behaviour of the electron and ion temperatures can be described by the equations in (2).

These equations describe the changes in energy of the electrons and ions (subscripts e and i) with heat capacities C_e and C_i. These changes come from heat conduction, $\nabla\cdot\mathbf{K}_a$, with $a = e$ or i, and electron-ion energy exchange, $G(T_e)\cdot(T_e - T_i)$. Because the energy transfer depends on electron-ion collisions the factor G is assumed to depend only on T_e [34]. However, an explicit dependance on T_i is found within models considering coupled electron-ion modes [35, 36]. In this case, the occurrence of ion acoustic modes depends on the ion temperatures [37].

In the system studied here, the timescales are sufficiently small that the conduction terms $\nabla\cdot\mathbf{K}_e$ and $\nabla\cdot\mathbf{K}_i$ can be ignored, as they take values of $\sim 10^3$ W compared to $\sim 10^{10}$ W from the electron-ion term. This means that the behaviour of the system is controlled solely by the electron-ion coupling factor $G(T_e)$. Previous work (e.g., Ref. [18]) has treated this as a fitting parameter, but here the electron-ion coupling is calculated from the density of states and occupation numbers for tantalum as a func-

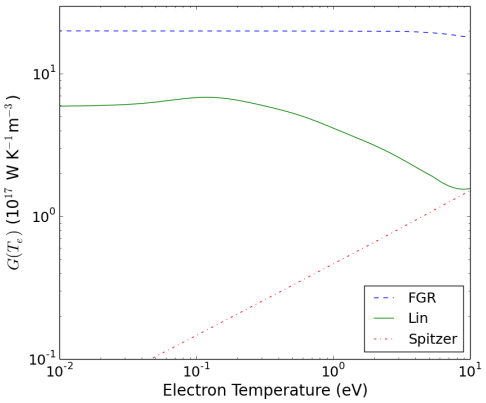

Figure 4: Values of $G(T_e)$ relevant for the conditions reached in this experiment, calculated using formula from Lin [22] and DOS from *ab initio* MD simulation. Values calculated using Fermi Golden Rule (FGR) and Spitzer plasma models are plotted for comparison.

tion of T_e. Using the relation from [22], we have:

$$G(T_e) = G_0 \int_{-\infty}^{\infty} \frac{g^2(E)}{g^2(E_F)} \left(-\frac{\partial\left[f(E,T_e)\right]}{\partial E} \right) dE, \quad (3a)$$

$$G_0 = \pi \hbar k_B \lambda \langle \omega^2 \rangle g(E_F) \quad (3b)$$

This formula shows that the electron-ion coupling depends on the density of states, $g(E)$, and the occupation, assumed to be a finite temperature Fermi distribution $f(E, T_e)$. The value at $T_e = 0$, which we refer to as G_0, depends on the occupation at the Fermi energy, E_F, and on the second moment of the phonon spectrum, $\langle \omega^2 \rangle$. The latter is approximated here as $\Theta_D^2/2$, and on the dimensionless electron-phonon coupling constant λ, which is commonly used in solid-state physics (see e.g. Ref. [38]) to compare coupling strengths in different materials. The value used here, $\lambda = 0.65$, was taken from McMillan [40].

Other models for the electron-ion coupling strength include the Spitzer formula [39] and the Fermi Golden Rule (FGR) [35]. Values from these are presented in Figure 4 as well.

4. Results and Discussion

To improve the signal to noise ratio on the image plate, we subtracted the averaged background on either side of the diffracted K-α line shown in Figure **??**. This was then further smoothed over a 30 μm length due to

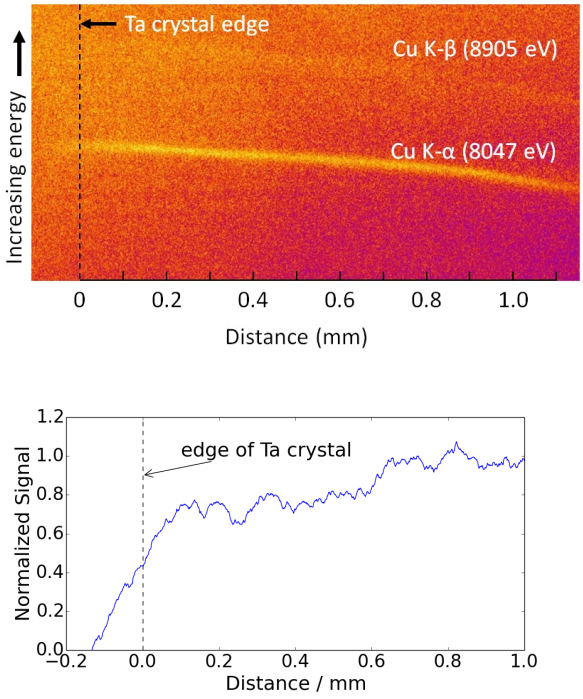

Figure 5: Data from the image plate observing the K-α Bragg line diffracted from the Ta crystal at (200). a) Raw data, with both K-α and K-β lines visible. The signal which appears to extend beyond the crystal edge is due to averaging over the finite source size. b) Lineout along the K-α Bragg line, with data normalized to the height of the signal in the unheated region.

the finite size of the x-ray source. The signal was integrated across the width of the diffracted line, with different choices of the width giving only minor (<5%) corrections from the values shown in Fig. **??**. Imperfections in the crystal surface and inhomogeneities in the proton beam spectrum uniformity acount for the sparial variations of the signal. From the deviation of the signal around a fitted curve, we estimate an overall error in this data of 11.8%. These values are normalized relative to the signal from the unheated region, and converted into the temperature across the width of the crystalline sample as described by Eq. (1); this is shown in Figure 6. The error in the temperature is also reported in the plot. The temperature is expected to decrease from a maximum to just above ambient temperature, and it can been seen in Figure 6 that it does tend toward this value.

The additional lines shown in Figure 6 are the temperatures at the front surface of the metal, as predicted from the measured proton spectrum and coupling values

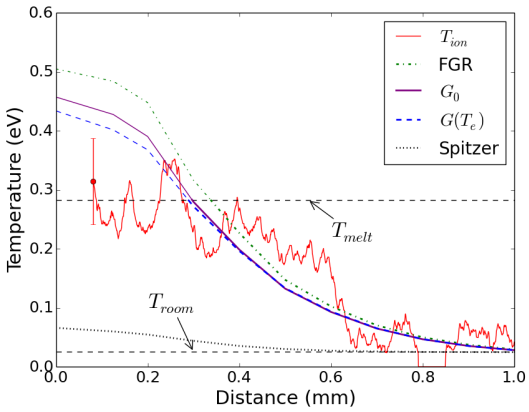

Figure 6: Ion temperature measured across the sample at a delay of 70 ps from proton creation, in red. Other lines show the expected temperatures from the measured proton spectrum and varying coupling models: Fermi Golden Rule (FGR), Spitzer, and the formula from Lin with $\lambda = 0.65$ [40], with and without temperature dependence. Values above the melt temperature are calculated in the same way, neglecting the changes in C_e and $G(T_e)$ that would occur.

given in Equation (3), as well as using other theoretical models. The extinction length of the x-rays in tantalum is sufficiently small (0.4 μm) that the front surface temperature will dominate the diffraction strength. The rising temperature towards the centre of the spot is due to the proton time of flight (TOF); at the probed delay (70 ps) the only protons which have reached points at the edge of the proton-heated spot are the high-energy tail (>10 MeV), which do not deposit energy as efficiently as lower energy protons.

The general impression of comparing the predicted and measured values of temperature is that the same trend is observed, with all of the coupling models except for Spitzer's formula giving values which agree with the experimental result within the margin of error. The fact that this is not true near the centre of the spot is due to the sample beginning to melt. Therefore, a diffraction-based measurement is no longer appropriate.

Since the error bars on the data are large, care must be taken when drawing conclusions. We are confident in saying that the much lower coupling strengths predicted by Spitzer are incorrect, as the temperatures these predict are well outside the data observed, therefore we can put a lower limit on the coupling needed to explain the observed results. Calculations performed with higher values of λ made increasingly little difference and gave

Sample	**Heating**	**τ (ps)**	**G_0 ($WK^{-1}m^{-3}$)**
Graphite [18]	Protons	150 (*)	$5.4 - 6.6 \times 10^{15}$
Graphite [19]	Electrons	450 (*)	2×10^{15}
Graphite [20]	X-rays	0.032 (*)	2.7×10^{19} (*)
Silicon [16]	Shock	200 (*)	1×10^{16}
Aluminium [17]	Shock	900 (*)	2.1×10^{15} (*)
Aluminium [41]	Laser Irradiation	< 1	3.1×10^{17} (*)
Gold [42]	Laser Irradiation	3.5 (*)	2.8×10^{16}
Gold [43, 44]	Laser Irradiation	5	1.96×10^{16} (*)
Tantalum	Protons	< 0.5	$> 3.08 \times 10^{17}$

Table 1: Comparison of coupling strengths and corresponding characteristic equilibration times ($\tau = C_e/G_0$) from this work, and previous work on graphite and metallic samples. Metals can be seen to generally couple more strongly.
(*) *Inferred from values given in the reference.*

similarly good fits, which is to be expected: at these coupling strengths, the electron and ion temperatures remain similar throughout the evolution, because the rate of energy deposition due to proton TOF is comparable to the equilibration time.

The equilibration of electron and ion temperatures is a complex subject in WDM research. In Table I we have compiled a summary of recent experimental results. They show large differences in the equilibration times, depending on the material and the heating mechanisms. The results we have obtained for the coupling strength in tantalum are high, although this is not unexpected from Eq. (3b) as it has a relatively high value of λ compared to other materials, as can be seen in Ref. [40]. However, other results e.g. those published in [17, 41] suggest that the formula reproduced here as Equation (3) is not universally applicable.

As explained in detail in the appendix to Ref. [22],

the formula assumes the high-temperature approximation to the Bose-Einstein distribution function, and would be significantly affected by changes to the density of states $g(E)$. The electron distribution changed from the assumed finite temperature Fermi distribution $f(E, T_e)$ would also make a difference [21], but only to the temperature-dependant part of (3). Although we are confident in these assumptions for our work here, situations where they are not applicable would require a different model.

5. Conclusion and Future Work

From the results presented here, we can conclude that the values of electron-ion coupling in tantalum are significantly higher than in graphite, and do not contradict the theoretical predictions by earlier work [22]. However, the uncertainty in the temperature measurements are not sufficiently low for $G(T_e)$ to be exactly inferred from the results, so instead only a lower bound of $G_0 > 3.08\times10^{17}$ can be placed on the coupling strength.

The model used, while appropriate here, is not generally applicable and consequently more work is still needed for a more complete understanding of interspecies energy transfer pathways.

Acknowledgements

The authors gratefully acknowledge the help received from JLF staff in obtaining the results presented. This work was supported in parts by EPSRC grant EP/G007187/1 and by the Science and Technology Facilities Council of the United Kingdom. Additional support from AWE plc is also acknowledged.

References

[1] M. W. C. Dharma-Wardana, Phys. Rev. E 86 (2012) 036407.
[2] B. Holst, et al., Phys. Rev. B 90 (2014) 035121.
[3] H. Rüter, R. Redmer, Phys. Rev. Lett. 112 (2014) 145007.
[4] J. Vorberger, et al., Phys. Rev. Lett. 109 (2012) 225001.
[5] S. White, et al., High Enery Density Physics 9 (2013).
[6] D. Kraus, et al., Phys. Rev. Lett. 111 (2013) 255501.
[7] B. Cho, et al., Phys. Rev. Lett. 106 (2011) 167601.
[8] U. Zastrau, et al., Phys. Rev. Lett. 112 (2014) 105002.
[9] L. Fletcher, et al., Phys. Rev. Lett. 112 (2014) 145004.
[10] J. Lindl, O. Landen, J. Edwards, E. Moses, Physics of Plasmas 21 (2014)
[11] O. A. Hurricane, et al., Nature 506 (2014) 7488.
[12] N. Nettelmann, Astrophysics and Space Sci. 336 (2011) 1.
[13] B. Militzer, et al., Astrophys. J. Lett. 688 (2008) L45.
[14] J. Vorberger, D.O. Gericke, High Energy Density Physics 10 (2014).
[15] R. P. Drake, High Energy Density Physics, Springer-Verlag, Berlin, 2006.
[16] P. Celliers, A. Ng, G. Xu, A. Forsman, Phys. Rev. Lett. 68 (1992) 2305.
[17] D. Riley, N. C. Woolsey, D. McSherry, I. Weaver, A. Djaoui, E. Nardi, Phys. Rev. Lett., 84 (2000) 1704.
[18] T. G. White, et al., Sci. Rep. 2 (2012).
[19] T. G. White, et al., Phys. Rev. Lett. 112 (2014) 145005.
[20] S. Hau-Riege, et al., Phys. Rev. Lett. 108 (2014) 217402.
[21] B. Y. Mueller, B. Rethfeld, Phys. Rev. B 87 (2013) 035139.
[22] Z. Lin, L. Zhigilei, V. Celli, Phys. Rev. B 77 (2008) 075133.
[23] M. Passoni, L. Bertagna, A. Zani, New J. Phys. 12 (2010) 045012.
[24] F. Nürnburg, et al., Rev. Sci. Ins. 80 (2009) 033301.
[25] J. Fuchs, et al., Nat. Phys. 2 (2005) 101038.
[26] W. Murphy, A. Higginbotham, J. Wark, N. Park, Phys. Rev. B 78 (2008) 014109.
[27] D. Salzmann, Atomic Physics in Hot Plasma, Oxford University Press, Oxford, 1998.
[28] B. E. Warren, X-ray Diffraction, Addison-Wesley, Reading, MA, 1969.
[29] X. Gonze, et al., Comp. Phys. Commun. 180 (2009) 258.
[30] M. Torrent, F. Jollet, F. Bottin, G. Zérah, X. Gonze, Comp. Phys. Commun. 42 (2008) 337.
[31] F. Bottin, S. Leroux, A. Knyazev, G. Zérah, Comp. Mat. Sci. 42 (2008) 329.
[32] S. Anisimov, et al., Sov. Phys. JETP 39 (1974).
[33] Z. Chen, et al., Phys. Rev. Lett. 110 (2013) 135001.
[34] P. B. Allen, Phys. Rev. Lett. 59 (1987) 1460.
[35] M. Dharma-Wardana and F. Perrot, Phys. Rev. E 58 (1998) 3705.
[36] J. Vorberger, et al., Phys. Rev. E 81 (2010) 046404.
[37] J. Vorberger, D. Gericke, Phys. Plasmas 16 (2009) 082702.
[38] C. Leem, et al., Phys. Rev. Lett. 100 (2008) 016802.
[39] L. Spitzer, Physics of Fully Ionized Gases, Interscience, New York, NY, 1962.
[40] W. L. McMillan, Phys. Rev. 167 (1968) 2.
[41] B. Rethfeld, A. Kaiser, M. Vicanek, G. Simon, Phys. Rev. B 65 (2002) 214303.
[42] R. Ernstorfer, et al., Science 323 (2009) 5917.
[43] M. Nicoul, U. Shymanovich, A. Tarasevitch, D. von der Linde, K. Sokolowski-Tinten, App. Phys. Lett. 98 (2011).
[44] T. G. White, et al., Phys. Rev. B 90 (2014) 014305.

LLNL-JRNL-686300

This work performed under the auspices of the U.S. Department of Energy by Lawrence Livermore National Laboratory under Contract DE-AC52-07NA27344.